Measuring Attractive Interaction between a Self-Electrophoretic Micromotor and a Wall

Yankai Xu,[1] Chang Liu,[1] Jiayu Liu,[2] Pengzhao Xu,[2] Zuyao Xiao,[2] Wei Wang,[2,*] and H. P. Zhang[1,†]
[1]School of Physics and Astronomy, Institute of Natural Sciences and MOE-LSC, Shanghai Jiao Tong University, Shanghai 200240, China
[2]School of Materials Science and Engineering, Harbin Institute of Technology (Shenzhen), Shenzhen 518055, China

(Received 9 May 2024; revised 9 September 2024; accepted 18 November 2024; published 18 December 2024)

Chemically driven micromotors exhibit a pronounced affinity for nearby surfaces, yet the quantification of this motor-wall interaction strength remains unexplored in experiments. Here, we apply an external force to a self-electrophoretic micromotor which slides along a wall and measures the force necessary to disengage the motor from the wall. Our experiments unveil that the required disengaging force increases with the strength of chemical driving, often surpassing both the motor's effective gravity and its propulsive thrust. Experimental results are reproduced by an electrokinetic numerical model that incorporates fully resolved double layers. The model delineates that the attractive force emerges from the accumulation of excessive protons between the motor and the wall, thereby exposing a nonequilibrium mechanism that engenders attractive interactions between objects of like charge.

DOI: 10.1103/PhysRevLett.133.258304

Micromotors represent a fascinating category of colloidal particles endowed with the remarkable ability to propel themselves by harnessing energy from their surroundings [1–7]. For instance, Janus motors, with chemical reactions occurring on their surfaces, generate physical fields that drive their movement via phoretic mechanisms [8–13]. Owing to this capability for active motion at the microscopic scale, chemical micromotors find diverse applications in both biomedical and environmental contexts [14–19].

Micromotors are often deployed within confined environments, such as lab-on-a-chip devices [20] or within organisms [21]. The presence of confining boundaries perturbs the chemical, electrostatic, and hydrodynamic fields surrounding the motor. These disturbances, in turn, intricately couple back to the motor, significantly influencing its motion and giving rise to dynamic interactions between the micromotor and the confining wall [22–24]. For instance, through motor-wall interactions, micromotors can engage in steady-state sliding motion, where the micromotor moves parallel to the wall while maintaining a constant distance and orientation relative to the surface normal [25–36]. Such wall-following behavior has proven invaluable for controlling and rectifying micromotor motion [25,27,29,32–34,37]. Moreover, motor-wall interactions give rise to other significant phenomena, including variations in motor speed [20,38–40] and rheotaxis [31,33].

Despite the recognized significance of motor-wall interaction, the direct measurement of interaction strength remains an unaddressed challenge in experimental studies. To address this issue, we fabricate TiO_2-Pt Janus micromotors equipped with a superparamagnetic core. Leveraging this core, we exert an external force on a sliding motor and measure the force necessary for its disengagement from the wall. Our experiments reveal that the required disengaging force increases with the intensity of chemical driving, often exceeding the combined effects of gravity and propulsive force. These findings find support in an electrokinetic numerical model that fully resolves the double layers.

We employ a standardized synthesis procedure to produce core-shell microspheres [41]. Initially, superparamagnetic Dynabead microspheres, measuring 2.8 μm in diameter, serve as the core onto which TiO_2 nanoparticles are uniformly deposited, forming a TiO_2 shell with a thickness of 30 nm. Subsequently, Pt is sputtered onto half of the resulting Dynabead-TiO_2 core-shell microspheres, as illustrated in Fig. 1(a).

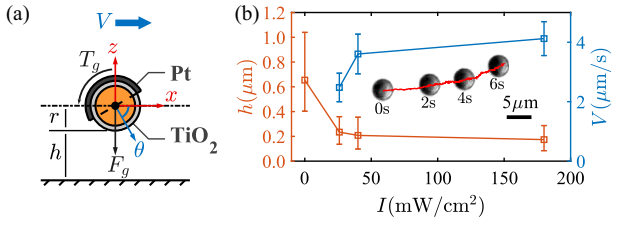

FIG. 1. (a) Diagram illustrating a TiO_2-Pt motor in sliding state, characterized by its height h, speed V, and tilt angle θ. The effective gravity and torque are denoted as F_g and T_g, respectively. The Dynabead core and TiO_2 and Pt layers are distinguished by different colors. (b) Motor speed and height as a function of UV intensity I. Inset: four images of a sliding motor.

*Contact author: weiwangsz@hit.edu.cn
†Contact author: hepeng_zhang@sjtu.edu.cn

We disperse the micromotors in a 50 mM hydroquinone solution and enclose the sample within a silicon chamber with glass top and bottom surfaces. Unless stated otherwise, measurements are carried out on motors moving along the bottom glass slides. Under UV illumination, hydroquinone undergoes photocatalytic oxidation to benzoquinone (BQ) on the TiO_2 side (anode: $QH_2 + 2h^+ \rightarrow BQ + 2H^+$), while concurrently reducing back to hydroquinone on the Pt-coated side (cathode: $BQ + 2H^+ + 2e^- \rightarrow QH_2$) [41]. These photocatalytic chemical reactions generate a proton gradient and drive the micromotors into motion, which is recorded using a 40× or 20× objective at a rate of 20 or 66 frames/ sec with a camera.

We use a standard particle-tracking algorithm to extract 2D motor trajectories from raw videos and compute mean-square displacement (MSD) from the tracking results. In the short-time regime ($t \ll 1/D_r$), we fit the MSDs with the equation: $\Delta r^2 = 4D_0 t + V^2 t^2$, where V is the propulsion speed and D_0 is the thermodynamic diffusivity. Here, $D_r = k_B T/8\pi\eta r^3$ denotes the bulk rotational diffusion coefficient, with r the radius, η the viscosity, k_B the Boltzmann constant, and T the temperature. Since thermodynamic diffusivity D_0 is linked, via the fluctuation-dissipation theorem, to its hydrodynamic friction coefficient, which depends on the motor height h [defined in Fig. 1(a)], we can estimate h through D_0 [42–44], as shown in Sec. I(C) in Supplemental Material [45]. We measure the motor speed V and height h at different UV intensities, which control reaction rate. As shown in Fig. 1(b), in the absence of UV light ($I = 0$), the motor is in thermal equilibrium and maintains a height of 0.65 μm, set by the balance of the motor's effective gravity and electrostatic repulsion between the negatively charged motor and wall. Upon activation of UV light, we observe a reduction of the motor height to approximately 0.2 μm, which remains relatively constant for a range of motor speed from $V = 2.4$ μm/s (at $I = 26$ mW/cm^2) to $V = 4.3$ μm/s (at $I = 180$ mW/cm^2) [42]. Motor tilt angle θ is estimated from micrographs of TiO_2-Pt motors with SiO_2 cores. As shown in the inset of Fig. 1(b), opaque Pt coating generates a distinctive dark region and analysis of its shape leads to an estimation of $\theta = 30.96 \pm 6.87°$; see Sec. I(E) in Supplemental Material [45] for details.

To show the motor-wall interaction, we carry out experiments on the ceiling of the sample chamber. Figure S10 and Video S1 in the Supplemental Material [45] depict that, under UV illumination, TiO_2-Pt motors robustly slide on the ceiling, demonstrating that the attractive force is sufficiently large to counteract the motor gravity. The motor-wall attraction also provides a plausible explanation to the observation, in Fig. 1(b), that the height h of a self-propelling motor is notably smaller than its equilibrium height.

We next apply a magnetic force to the motor via its paramagnetic core. As illustrated in the inset of Fig. 2(a), a permanent magnet is affixed to a precision linear stage inclined at a 45° angle relative to the horizontal direction. We regulate the magnetic force by adjusting the separation between the magnet and the sample, denoted as Δ; see Sec. I(G) in Supplemental Material for details [45]. In an experiment conducted with $I = 180$ mW/cm^2, we incrementally increase the z component of the magnetic force F_{Mz} from 0.05 to 0.4 pN by decreasing Δ from 30 to 15 mm. While ramping up F_{Mz}, holographic microscopy captures the 3D coordinates of the motors. The height h data obtained from three motors are depicted as blue curves in Fig. 2(a), alongside the magnetic force F_{Mz} represented by the orange line. Initially, when F_{Mz} is small, all three motors remain close to the wall. However, at $t = 5$ sec (corresponding to $F_{Mz} = 0.17$ pN), the first motor begins to detach from the wall. Subsequently, the second and third motors disengage from the wall at $t = 7.5$ sec ($F_{Mz} = 0.19$ pN) and $t = 25.5$ sec ($F_{Mz} = 0.37$ pN), respectively. For each motor trajectory, we record the magnetic force F_{Mz} at the moment of disengagement and define this force as the critical disengaging force f_c. At every UV intensity I, we measure f_c for approximately 40 motors and plot the mean and variance of f_c against the mean motor velocity V at this I. The data presented in Fig. 2(b) reveal that f_c increases with V and exhibits significant variability. Notably, f_c measured at $V = 4.3$ μm/s can be larger than the particle's effective gravity (0.1 pN) and propulsion force (0.2 pN, estimated from the motor velocity and frictional coefficient).

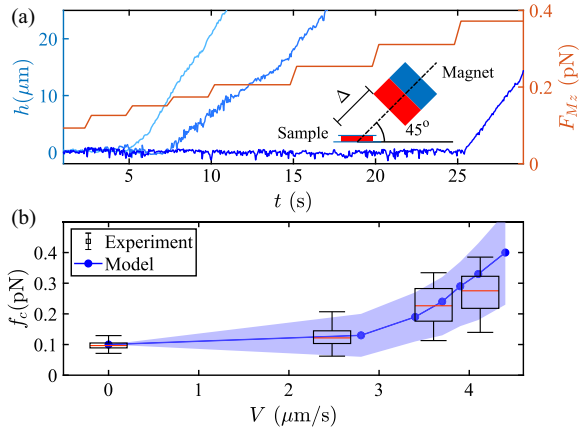

FIG. 2. (a) Temporal records of applied magnetic force (orange line) and motor height data (blue lines) obtained from an experiment conducted with $I = 180$ mW/cm^2. The inset graph provides an illustration of the experimental setup. (b) Critical disengaging force plotted as a function of the mean motor speed. Each data point represents measurements taken at a specific UV intensity. The red lines and box limits in the box plots denote the medians and quartiles, respectively, while the whiskers extend up to 1.5× the interquartile range. The blue dots represent results obtained from the numerical model, and the shaded blue area indicates numerical variability. See Videos S2 and S3 in the Supplemental Material [45] for motor trajectories in magnetic field.

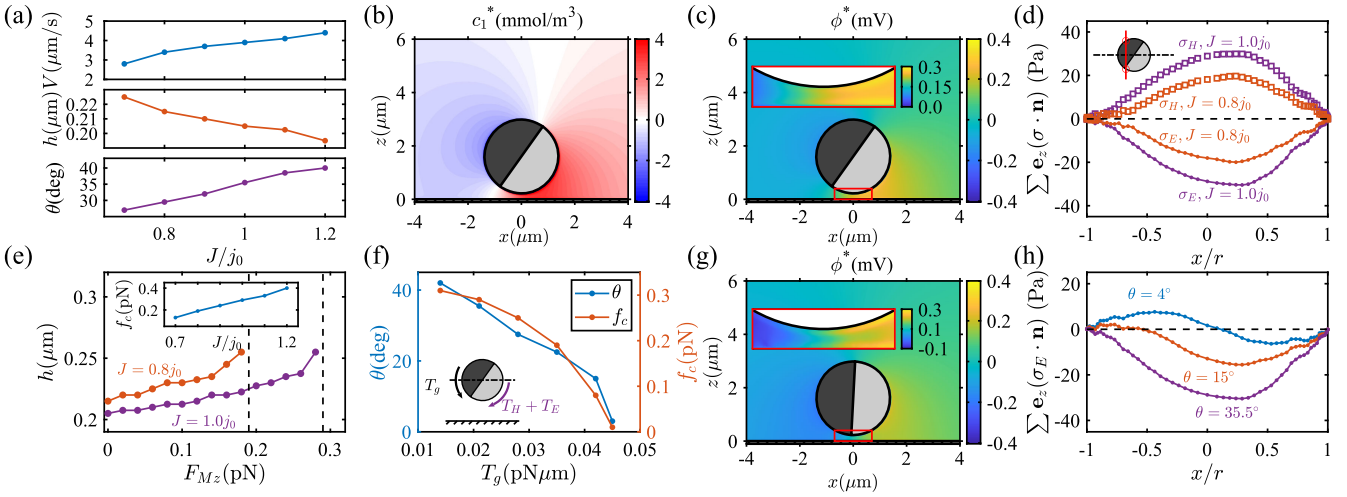

FIG. 3. Numerical results. (a) Motor velocity, height, and angle computed at different proton fluxes. (b),(c) Background-subtracted proton concentration c_1^* and electrostatic potential ϕ^* fields around a motor with a tilt angle $\theta = 35.5°$. (d) Profiles of z component of the electrostatic traction $\sum \mathbf{e}_z \cdot (\sigma_E \cdot \mathbf{n})$ and hydrodynamic traction $\sum \mathbf{e}_z \cdot (\sigma_H \cdot \mathbf{n})$ as a function of x coordinate. (e) Motor height h as a function of the magnetic force F_{Mz} computed with two proton fluxes. The dashed lines mark the critical disengaging force f_c. Inset: f_c as a function of the proton fluxes. (f) Tilt angle θ and critical disengaging force f_c as a function of the gravitational torque T_g. Inset: the gravitational torque T_g balances the sum of hydrodynamic torque T_H and electrostatic torque T_E. (g) Background-subtracted electrostatic potential computed with $T_g = 0.045$ pN μm, resulting in a small tilt angle $\theta = 4°$. (h) The electrostatic traction profiles in sliding states with different tilt angle θ. These states are generated with $T_g = 0.021$, 0.042, and 0.045 pN μm, respectively. Proton flux has a unit of $j_0 = 10^{-5}$ mol/m^2/s. The inset of (c) and (g) magnifies the gap between the motor and the wall. All parameters not specified use default values in Supplemental Material, Table S2 [45].

To elucidate the motor-wall attraction, we employ a 2D numerical model solving the Poisson-Nernst-Planck-Stokes equations [62–69]. Our steady-state model operates under small Péclet and Reynolds numbers. The ion concentration fields are governed by the Nernst-Planck equation: $\nabla \cdot \mathbf{J}_i = 0$ and $\mathbf{J}_i = -D_i \nabla c_i - z_i F \nu_i c_i \nabla \phi$, where $\mathbf{J}_i$ is the flux, D_i the diffusivity, ν_i the mobility, z_i the valence, F Faraday's constant, ϕ the electrostatic potential, and subscript i denotes ion species. The electrostatic potential is related to the local free charge density by the Poisson equation: $-\varepsilon \nabla^2 \phi = F \sum z_i c_i$, where ε is the liquid's permittivity. Fluid motion is described using the Stokes equations: $-\nabla p + \eta \nabla^2 \mathbf{u} = F \sum z_i c_i \nabla \phi$ and $\nabla \cdot \mathbf{u} = 0$, where p is the pressure.

Our model is driven by the chemical reactions on the motor surface. We prescribe equal and opposite proton fluxes (J and $-J$) normal to the TiO_2 and Pt surfaces; other ion fluxes are set to zero. At the motor surface, we apply the no-slip condition for fluid velocity and specify the local surface potential as $\phi = \zeta_m$. On the wall, chemical fluxes are zero, electrostatic potential is $\phi = \zeta_w$, and no-slip flow condition is applied. At the exterior boundaries of the computation domain, we set zero potential, zero flow velocity, and bulk ion concentrations $c_i = c_{\mathrm{bulk},i}$.

We utilize a finite-element method to solve the model. From the solutions of physical fields, the electrostatic and hydrodynamic force and torque on the motor can be computed via Maxwell σ_E and hydrodynamic σ_H stress tensors. Total force and torque on the motor, $\mathbf{F}_{\mathrm{tot}}$ and $\mathbf{T}_{\mathrm{tot}}$, are calculated by combining these results with the external forces and torques generated by gravity and magnetic field. We design an iterative procedure to find the motor parameters in a sliding state by changing V, θ, and h to reduce the magnitudes of the total force $|\mathbf{F}_{\mathrm{tot}}|$ and torque $|\mathbf{T}_{\mathrm{tot}}|$; the procedure stops when $|\mathbf{F}_{\mathrm{tot}}|$ and $|\mathbf{T}_{\mathrm{tot}}|$ are below a threshold. See Sec. II of Supplemental Material for model details [45].

We employ the model to investigate the sliding state without external magnetic field. The proton flux J is varied to simulate the effect of UV intensity. As depicted in Fig. 3(a), both the motor velocity V and tilt angle θ increase with J, while the motor height h slightly decreases. At $J = 1.0 \times 10^{-5}$ mol/m^2/s, the model predicts $V = 3.9$ μm/s, $\theta = 35.5°$, and $h = 0.2$ μm, consistent with experimental measurements at $I = 180$ mW/cm^2 in Fig. 1. We utilize the proton concentration and potential fields to elucidate the mechanism of motor-wall interaction. For clarity, we remove the sharp changes of fields in the double layer by subtracting background fields in the absence of chemical reactions from instantaneous fields. The background-subtracted fields, denoted by c_1^* and ϕ^*, are plotted in Figs. 3(b) and 3(c). Figure 3(c) reveals a pronounced accumulation of protons within the gap region between the motor and the wall, with the TiO_2 side tilting downward, leading to an increase of potential (positive ϕ^*). Conversely, the opposite occurs on the Pt side, as shown by negative c_1^* and ϕ^*. From

the potential field, we further compute the z component of the electrostatic traction $\mathbf{e}_z \cdot (\sigma_E \cdot \mathbf{n})$ on the motor surface and sum traction values at two points with the same x coordinate to obtain a profile [inset of Fig. 3(d)]. Results in Fig. 3(d) depict a downward electrostatic force on the motor, leading to an attraction to the wall. Hydrodynamic traction profiles in Fig. 3(d) have positive values, indicating a repulsive contribution.

We perturb the motor's sliding state in models with an external force, mimicking experiments in Fig. 2. As depicted in Fig. 3(e), the motor height h increases with the applied force F_{Mz} and the sliding state cannot be sustained when F_{Mz} exceeds a critical threshold f_c, denoted by dashed lines. The inset of Fig. 3(e) shows that f_c rises with the driving proton flux J. In Fig. 2(b), we plot f_c against the motor velocity V computed with the same J, revealing that the numerical results from our 2D model are consistent with experimental measurements.

We conduct a thorough investigation into how various factors, such as motor diameter, zeta potential, and gravitational torque, influence motor-wall attraction. This attraction reliably occurs across a broad spectrum of conditions provided that the tilt angle θ remains positive. To illustrate this, we increase the gravitational torque [Fig. 3(f) inset], causing the motor to rotate clockwise. This rotation reduces θ until a balance is achieved among gravitational, hydrodynamic, and electrostatic torques. As shown in Fig. 3(f), the critical force f_c diminishes as θ nears zero. In setups where θ is minimal, the anode faces forward rather than toward the wall [Fig. 3(g)]. This alignment leads to a neutralization of the attractive force between the anode and wall due to the repulsive forces acting on the cathode. As a result, the total attraction significantly weakens [Fig. 3(h)].

The experimentally measured f_c in Fig. 2(b) displays significant variability. This is likely due to the fact that Dynabeads possess a small permanent magnetic moment [70], allowing the external magnetic field to exert a torque on the magnetic core. We incorporate this magnetic torque into our model and demonstrate its ability to increase/decrease f_c by increasing/decreasing the motor's tilt angle, as illustrated by the shaded blue area in Fig. 2(b); see Sec. II(J) of Supplemental Material for details [45].

In addition to spherical micromotors, we investigate the behavior of bimetallic (Au-Rh) microrods. In our experimental setup, these microrods propel themselves within a sample cell containing an H_2O_2 solution and a circular structure. Unlike previous studies [20,25,32], our observations take place in a custom microscope setup with a horizontal optical axis [Fig. S1(a) [45]]. This setup allows the microrods to move under the influence of gravity. As illustrated in Fig. 4(a), the microrods demonstrate the ability to overcome gravitational forces and traverse along the structure for extended periods. As the fuel gradually depletes over time, we observe a corresponding decrease in the microrods' speed. Eventually, the microrod disengages

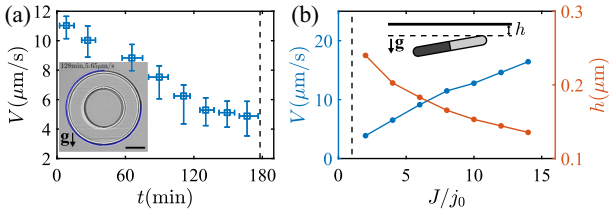

FIG. 4. (a) Temporal record of microrod speed as the fuel in the chamber depletes, observed around a circular structure. The dashed line indicates the moment when the microrod detaches from the structure. Inset: a trajectory spanning 16.67 sec is overlaid on an image of the structure, with gravity pointing downward in the image. The scale bar represents 10 μm. (b) Numerical results from a microrod moving on the ceiling, as depicted schematically in the inset. Motor velocity and height are computed at various proton fluxes, with dashed lines indicating the critical proton flux where a sliding state on the ceiling cannot be sustained.

from the structure as its speed reaches around 4.5 μm/s. To complement the experiment, we conduct model calculations to explore the sliding behavior of a microrod on the ceiling [inset of Fig. 4(b)]. By simulating a reduction in proton flux to mimic the depletion of H_2O_2 fuel, we observe that the microrod fails to maintain a stable sliding state on the ceiling when its speed drops below 4 μm/s, consistent with our experimental findings.

Strong motor-wall attraction observed with both spherical and rod-shaped motors suggests that such attraction may be common in self-electrophoretic motors [20,41,71–76]. Numerical simulations reveal the following picture: when the proton-releasing anode is oriented toward the boundary, protons accumulate in the gap between the motor and the wall, raise the local electrostatic potential, and engender an attractive force. This picture may also provide fresh insights into the frequently observed wall-following behavior in Pt-insulator [polystyrene (PS), SiO_2, or 3-(trimethoxysilyl)propyl methacrylate] systems [27,29,30,34,35,37]. Traditionally, this behavior has been interpreted within the framework of neutral self-diffusiophoresis [27,29,35]. However, recent studies have shown that the self-electrophoretic mechanism may operate in these systems [77–80] with an inhomogeneous flux distribution, where proton dynamics occurs on the Pt-covered part, with the motor pole serving as the cathode and the equator as the anode. Electrophoretic model calculations in Sec. II(O) in Supplemental Material [45] show strong motor-wall attraction with inhomogeneous flux distribution. Consequently, the observed wall-following motility in Pt-insulator systems may, to some extent, be attributed to the electrostatic mechanism revealed in the current Letter. We also investigate an ionic diffusiophoretic PS-Ag system [67–69,80–83]. Figure S10(c) [45] shows PS-Ag motors can slide on the ceiling against gravity, demonstrating a strong motor-wall attraction. Numerical

results in Sec. II(P) in Supplemental Material show the attraction may arise from the accumulation of the slowly diffusing positive ions in the gap between motor and wall.

In summary, we have developed spherical TiO_2-Pt micromotors featuring a superparamagnetic core. The core-shell design allows us to measure the force required to dislodge the sliding motors from the wall. Our experiments revealed a strong motor-wall attraction. By using an electrokinetic numerical model, we replicated these experimental results and showed that the attraction may be attributed to the accumulation of protons between the motor and the wall. Subsequent experiments and simulations have corroborated this mechanism in a bimetallic rod system. These findings imply that ions generated by chemical reactions may be harnessed to regulate interactions among charged entities [84–88]. This nonequilibrium mechanism holds significant potential for steering interactions across a diverse array of systems.

Acknowledgments—We acknowledge financial support of the NSFC (No. 12225410, No. 12074243, and No. T2322006), the Shenzhen Science and Technology Program (RCYX20210609103122038, JCYJ20210324121408022), and the Student Innovation Center at Shanghai Jiao Tong University.

[1] W. Wang, W. Duan, S. Ahmed, T. E. Mallouk, and A. Sen, Nano Today **8**, 531 (2013).
[2] S. Sanchez, L. Soler, and J. Katuri, Angew. Chem., Int. Ed. **54**, 1414 (2015).
[3] J. Elgeti, R. G. Winkler, and G. Gompper, Rep. Prog. Phys. **78**, 056601 (2015).
[4] C. Bechinger, R. Di Leonardo, H. Löwen, C. Reichhardt, G. Volpe, and G. Volpe, Rev. Mod. Phys. **88**, 045006 (2016).
[5] J. Zhang, E. Luijten, B. A. Grzybowski, and S. Granick, Chem. Soc. Rev. **46**, 5551 (2017).
[6] P. Illien, R. Golestanian, and A. Sen, Chem. Soc. Rev. **46**, 5508 (2017).
[7] W. Wang, J. Am. Chem. Soc. **145**, 27185 (2023).
[8] W. F. Paxton, K. C. Kistler, C. C. Olmeda, A. Sen, S. K. St Angelo, Y. Y. Cao, T. E. Mallouk, P. E. Lammert, and V. H. Crespi, J. Am. Chem. Soc. **126**, 13424 (2004).
[9] S. Fournier-Bidoz, A. C. Arsenault, I. Manners, and G. A. Ozin, Chem. Commun. 441 (2005).
[10] Y. Wang, R. M. Hernandez, J. Bartlett, J. David, J. M. Bingham, T. R. Kline, A. Sen, and T. E. Mallouk, Langmuir **22**, 10451 (2006).
[11] J. R. Howse, R. A. L. Jones, A. J. Ryan, T. Gough, R. Vafabakhsh, and R. Golestanian, Phys. Rev. Lett. **99**, 048102 (2007).
[12] I. Buttinoni, J. Bialke, F. Kummel, H. Lowen, C. Bechinger, and T. Speck, Phys. Rev. Lett. **110**, 238301 (2013).
[13] J. Palacci, S. Sacanna, A. P. Steinberg, D. J. Pine, and P. M. Chaikin, Science **339**, 936 (2013).
[14] C. J. Wang, A. Bergmann, B. Lin, K. Kim, and A. Levchenko, Sci. Signal. (Online) **5**, ra17 (2012).
[15] W. Gao and J. Wang, ACS Nano **8**, 3170 (2014).
[16] Y. Alapan, O. Yasa, B. Yigit, I. C. Yasa, P. Erkoc, and M. Sitti, Annu. Rev. Control Rob. Auton. Syst. **2**, 205 (2019).
[17] C. Gao, Y. Wang, Z. Ye, Z. Lin, X. Ma, and Q. He, Adv. Mater. **33**, 2000512 (2021).
[18] H. Joh and D. E. Fan, Adv. Mater. **33**, 2101965 (2021).
[19] Z. Wu, Y. Chen, D. Mukasa, O. S. Pak, and W. Gao, Chem. Soc. Rev. **49**, 8088 (2020).
[20] C. Liu, C. Zhou, W. Wang, and H. P. Zhang, Phys. Rev. Lett. **117**, 198001 (2016).
[21] P. L. Venugopalan, B. E.-F. de Avila, M. Pal, A. Ghosh, and J. Wang, ACS Nano **14**, 9423 (2020).
[22] A. Mozaffari, N. Sharifi-Mood, J. Koplik, and C. Maldarelli, Phys. Fluids **28**, 053107 (2016).
[23] M. N. Popescu, W. E. Uspal, C. Bechinger, and P. Fischer, Nano Lett. **18**, 5345 (2018).
[24] Z. Xiao, M. Wei, and W. Wang, ACS Appl. Mater. Interfaces **11**, 6667 (2019).
[25] D. Takagi, J. Palacci, A. B. Braunschweig, M. J. Shelley, and J. Zhang, Soft Matter **10**, 1784 (2014).
[26] W. E. Uspal, M. N. Popescu, S. Dietrich, and M. Tasinkevych, Soft Matter **11**, 434 (2015).
[27] S. Das, A. Garg, A. I. Campbell, J. Howse, A. Sen, D. Velegol, R. Golestanian, and S. J. Ebbens, Nat. Commun. **6**, 8999 (2015).
[28] A. T. Brown, I. D. Vladescu, A. Dawson, T. Vissers, J. Schwarz-Linek, J. S. Lintuvuori, and W. C. K. Poon, Soft Matter **12**, 131 (2016).
[29] J. Simmchen, J. Katuri, W. E. Uspal, M. N. Popescu, M. Tasinkevych, and S. Sanchez, Nat. Commun. **7**, 10598 (2016).
[30] K. Dietrich, D. Renggli, M. Zanini, G. Volpe, I. Buttinoni, and L. Isa, New J. Phys. **19**, 065008 (2017).
[31] Q. Brosseau, F. B. Usabiaga, E. Lushi, Y. Wu, L. Ristroph, J. Zhang, M. Ward, and M. J. Shelley, Phys. Rev. Lett. **123**, 178004 (2019).
[32] M. S. Davies Wykes, X. Zhong, J. Tong, T. Adachi, Y. Liu, L. Ristroph, M. D. Ward, M. J. Shelley, and J. Zhang, Soft Matter **13**, 4681 (2017).
[33] L. Q. Ren, D. K. Zhou, Z. M. Mao, P. T. Xu, T. J. Huang, and T. E. Mallouk, ACS Nano **11**, 10591 (2017).
[34] J. Katuri, D. Caballero, R. Voituriez, J. Samitier, and S. Sanchez, ACS Nano **12**, 7282 (2018).
[35] S. Das, Z. Jalilvand, M. N. Popescu, W. E. Uspal, S. Dietrich, and I. Kretzschmar, Langmuir **36**, 7133 (2020).
[36] S. Ketzetzi, M. Rinaldin, P. Droge, J. d. Graaf, and D. J. Kraft, Nat. Commun. **13**, 1772 (2022).
[37] L. S. Palacios, S. Tchoumakov, M. Guix, I. Pagonabarraga, S. Sanchez, and A. G. Grushin, Nat. Commun. **12**, 4691 (2021).
[38] T. Y. Chiang and D. Velegol, Langmuir **30**, 2600 (2014).
[39] M. Wei, C. Zhou, J. Tang, and W. Wang, ACS Appl. Mater. Interfaces **10**, 2249 (2018).
[40] S. Ketzetzi, J. de Graaf, R. P. Doherty, and D. J. Kraft, Phys. Rev. Lett. **124**, 048002 (2020).
[41] P. Xu, S. Duan, Z. Xiao, Z. Yang, and W. Wang, Soft Matter **16**, 6082 (2020).
[42] S. Ketzetzi, J. de Graaf, and D. J. Kraft, Phys. Rev. Lett. **125**, 238001 (2020).
[43] C. Ha, H. Ou-Yang, and H. K. Pak, Physica (Amsterdam) **392A**, 3497 (2013).

[44] P. Sharma, S. Ghosh, and S. Bhattacharya, Appl. Phys. Lett. **97**, 104101 (2010).

[45] See Supplemental Material at http://link.aps.org/supplemental/10.1103/PhysRevLett.133.258304, which includes Refs. [46–61], for detailed experimental and numerical procedure, additional experimental and numerical results, and videos from experiments and simulations.

[46] W. Wang, T.-Y. Chiang, D. Velegol, and T. E. Mallouk, J. Am. Chem. Soc. **135**, 10557 (2013).

[47] J. Liu, Z. Yang, Z. Yan, S. Duan, X. Chen, D. Cui, D. Cao, T. Kuang, X. Ma, and W. Wang, J. Am. Chem. Soc. **146**, 4221 (2024).

[48] M. Malinauskas, M. Farsari, A. Piskarskas, and S. Juodkazis, Phys. Rep. **533**, 1 (2013).

[49] M. Lavaud, T. Salez, Y. Louyer, and Y. Amarouchene, Phys. Rev. Res. **3**, L032011 (2021).

[50] Jacob, *Intermolecular and Surface Forces*, 2nd ed. (Academic Press, London, 1992).

[51] S. B. Jacob H. Masliyah, *Electrokinetic and Colloid Transport* (John Wiley & Sons, Inc., New York, 2005).

[52] G. M. Dougherty, K. A. Rose, J. B.-H. Tok, S. S. Pannu, F. Y. S. Chuang, M. Y. Sha, G. Chakarova, and S. G. Penn, Electrophoresis **29**, 1131 (2008).

[53] Z. Xiao, S. Duan, P. Xu, J. Cui, H. Zhang, and W. Wang, ACS Nano **14**, 8658 (2020).

[54] J. Sheng, E. Malkiel, and J. Katz, Appl. Opt. **45**, 3893 (2006).

[55] S.-H. Lee, Y. Roichman, G.-R. Yi, S.-H. Kim, S.-M. Yang, A. van Blaaderen, P. van Oostrum, and D. G. Grier, Opt. Express **15**, 18275 (2007).

[56] Z. H. Shah, S. Wang, L. Xian, X. Zhou, Y. Chen, G. Lin, and Y. Gao, Chem. Commun. **56**, 15301 (2020).

[57] J. L. Moran, P. M. Wheat, and J. D. Posner, Phys. Rev. E **81**, 065302(R) (2010).

[58] R. Golestanian, T. B. Liverpool, and A. Ajdari, New J. Phys. **9**, 126 (2007).

[59] A. Dominguez and M. N. Popescu, arXiv:2404.16435.

[60] Y. Ibrahim, R. Golestanian, and T. B. Liverpool, J. Fluid Mech. **828**, 318 (2017).

[61] P. Vanysek, Ionic conductivity and diffusion at infinite dilution, *Handbook of Chemistry and Physics*, 92nd ed. (CRC Press, Boca Raton, 2011), pp. (5-111)–(5-113).

[62] J. L. Moran and J. D. Posner, J. Fluid Mech. **680**, 31 (2011).

[63] J. L. Moran and J. D. Posner, Phys. Fluids **26**, 042001 (2014).

[64] A. T. Brown, W. C. K. Poon, C. Holm, and J. de Graaf, Soft Matter **13**, 1200 (2017).

[65] J. L. Moran and J. D. Posner, Annu. Rev. Fluid Mech. **49**, 511 (2017).

[66] A. M. Brooks, M. Tasinkevych, S. Sabrina, D. Velegol, A. Sen, and K. J. M. Bishop, Nat. Commun. **10**, 495 (2019).

[67] M. De Corato, X. Arque, T. Patino, M. Arroyoe, S. Sanchez, and I. Pagonabarraga, Phys. Rev. Lett. **124**, 108001 (2020).

[68] T. V. Nizkaya, E. S. Asmolov, and O. I. Vinogradova, Curr. Opin. Colloid Interface Sci. **62**, 101637 (2022).

[69] A. Shrestha and M. Olvera de la Cruz, Phys. Rev. E **109**, 014613 (2024).

[70] M. M. van Oene, L. E. Dickinson, F. Pedaci, M. Kober, D. Dulin, J. Lipfert, and N. H. Dekker, Phys. Rev. Lett. **114**, 218301 (2015).

[71] R. Dong, Q. Zhang, W. Gao, A. Pei, and B. Ren, ACS Nano **10**, 839 (2016).

[72] B. Dai, J. Wang, Z. Xiong, X. Zhan, W. Dai, C.-C. Li, S.-P. Feng, and J. Tang, Nat. Nanotechnol. **11**, 1087 (2016).

[73] L. L. Wang, M. N. Popescu, F. Stavale, A. Ali, T. Gemming, and J. Simmchen, Soft Matter **14**, 6969 (2018).

[74] J. Wang, Z. Xiong, X. Zhan, B. Dai, J. Zheng, J. Liu, and J. Tang, Adv. Mater. **29**, 1701451 (2017).

[75] W. F. Paxton, P. T. Baker, T. R. Kline, Y. Wang, T. E. Mallouk, and A. Sen, J. Am. Chem. Soc. **128**, 14881 (2006).

[76] P. M. Wheat, N. A. Marine, J. L. Moran, and J. D. Posner, Langmuir **26**, 13052 (2010).

[77] S. Ebbens, D. A. Gregory, G. Dunderdale, J. R. Howse, Y. Ibrahim, T. B. Liverpool, and R. Golestanian, Europhys. Lett. **106**, 58003 (2014).

[78] A. Brown and W. Poon, Soft Matter **10**, 4016 (2014).

[79] X. Lyu, X. Liu, C. Zhou, S. Duan, P. Xu, J. Dai, X. Chen, Y. Peng, D. Cui, J. Tang, X. Ma, and W. Wang, J. Am. Chem. Soc. **143**, 12154 (2021).

[80] Y. X. Peng, P. Z. Xu, S. F. Duan, J. Y. Liu, J. L. Moran, and W. Wang, Angew. Chem., Int. Ed. **61**, e202116041 (2022).

[81] M. Ibele, T. E. Mallouk, and A. Sen, Angew. Chem., Int. Ed. **48**, 3308 (2009).

[82] C. Zhou, H. P. Zhang, J. Y. Tang, and W. Wang, Langmuir **34**, 3289 (2018).

[83] A. Dominguez and M. N. Popescu, Curr. Opin. Colloid Interface Sci. **61**, 101610 (2022).

[84] A. E. Larsen and D. G. Grier, Nature (London) **385**, 230 (1997).

[85] J.-P. Hansen and H. Löwen, Annu. Rev. Phys. Chem. **51**, 209 (2000).

[86] T. M. Squires and M. P. Brenner, Phys. Rev. Lett. **85**, 4976 (2000).

[87] Y. Han and D. G. Grier, Phys. Rev. Lett. **91**, 038032 (2003).

[88] S. Wang, R. Walker-Gibbons, B. Watkins, M. Flynn, and M. Krishnan, Nat. Nanotechnol. **19**, 485 (2024).